Synthesis of Core–Shell Graphitic Carbon@Silica Nanospheres with Dual-Ordered Mesopores for Cancer-Targeted Photothermochemotherapy

Yi Wang,[‡] Kaiyuan Wang,[⊥] Ren Zhang,[‡] Xingang Liu,[‡] Xueying Yan,[⊥] Jianxin Wang,[†] Ernst Wagner,[§] and Rongqin Huang[†,*]

[†]Department of Pharmaceutics, School of Pharmacy, Key Laboratory of Smart Drug Delivery, Ministry of Education, Fudan University, Shanghai 201203, China, [‡]Center of Analysis and Measurement, Fudan University, Shanghai 200433, China, [§]Department of Pharmacy, Ludwig-Maximilians-Universitaet (LMU), Munich, 81377, Germany, and [⊥]School of Pharmacy, Heilongjiang University of Chinese Medicine, Harbin 150040, China

ABSTRACT Tumor site-directed multifunctional therapeutic platforms such as photothermochemotherapy that respond to tumor-focused physical and biological stimuli are highly demanded for effective cancer therapy. Herein, targeting peptide-conjugated core–shell graphitic carbon@silica nanospheres with dual-ordered mesopores (MMPS) were successfully fabricated and developed as antitumoral doxorubicin (DOX) delivery system (MMPSD) for synergistic targeted photothermal chemotherapy of breast cancer. The hydrophilic mesoporous silica shell guarantees good water dispersity of MMPSD. The hydrophobic graphitic mesoporous carbon core provides excellent hydrophobic drug loading, immediate contact between the drug and photothermal hotspots, and high NIR photothermal conversion efficiency. SP13 peptide facilitates MMPSD for targeted and enhanced delivery of DOX within HER2-positive SK-BR-3 breast cancer cells, while PEGylation ensures biocompatibility. Thus, the MMPSD system exhibited efficient drug loading capacity, high targeting ability, sensitive NIR/pH-responsive DOX release, sustained release, and excellent combined antitumor activity.

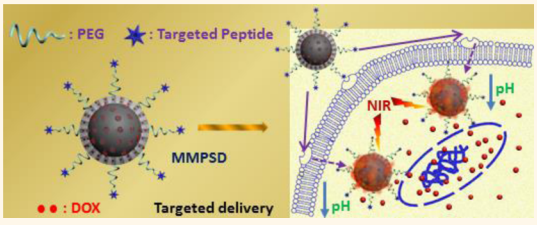

KEYWORDS: mesoporous silica · mesoporous carbon · core–shell · targeted delivery · combined therapy

Multifunctional photothermal chemotherapeutic platforms have received considerable attention in recent years since they can drastically overcome or reduce multidrug resistance, increase drug accumulation within targeted tumor, improve the anticancer therapeutic effect, and minimize the invasive damage to normal tissues.[1−5] sp^2-Hybridized carbon nanomaterials including fullerene, carbon nanotubes, and graphene have been widely exploited for chemotherapy or photothermal cancer therapy due to their unique physiochemical properties (*e.g.*, NIR absorption for photothermal heating and $\pi-\pi$ interaction for drug loading).[6−11] However, pristine carbon nanomaterials have two obvious disadvantages: (1) easy aggregation and low biocompatibility caused by high hydrophobicity;[12] (2) limited and unstable drug loading by mere surface adsorption.[13] To overcome these disadvantages, some improvements including oxidization or surface mesoporous coating have been induced to the pristine carbon nanomaterials.[13−15] Unfortunately, the destroyed sp^2-hybridized network caused by oxidation was not beneficial for NIR photothermal conversion. What's worse is that oxidation may create toxic impurities and increase the generation of reactive oxygen species (ROS), inducing cell oxidative stress.[12,16−18] Although surface mesoporous silica coating was a more effective improvement to the biocompatibility, drug loading, and post modification,[13,19] limited drug amounts can only be stored in the mesoporous silica coating and not be immediately contacted with the hotspots (graphitic carbon),

* Address correspondence to rqhuang@fudan.edu.cn.

Received for review March 18, 2014 and accepted July 21, 2014.

Published online July 21, 2014
10.1021/nn5027214

which was still not beneficial for the requirement of high dosage and NIR-mediated drug release.[20−22] In our previous work, template semigraphitized mesoporous silica (TsGMS) was used to directly contact the drug for combined photothermochemotherapy.[23] However, the high-temperature calcination for the semigraphitization depressed the hydrophilicity and further functionalization of mesoporous silica. Also, the amount of hotspots in TsGMS was limited, which resulted in a relatively lower photothermal conversion effect.[23] Recently, mesoporous carbon nanoparticles (MCN), as three-dimensional carbon materials, present an encouraging class of potential drug vehicles for cancer therapy attributed to their well-defined mesoporosity, large surface area, and high pore volume.[24,25] After graphitization under high temperature, graphitic MCN are more advantageous in some aspects compared to their counterpart carbon nanomaterials or even the extensively explored mesoporous silica nanoparticles (MSN). For example, (1) the mesopores with an sp^2-hybridized framework are favorable due to their high drug loading capacity, (2) the graphitic pore walls would possible be photothermal conversion hotspots for NIR-mediated photothermotherapy, and (3) the multiple-controlled drug release performances can also be easily achieved due to the immediate contact between the drug and the hotspots at the graphitic pore walls. However, very few studies concerning graphitic MCN for photothermal combined chemotherapy have been reported so far mainly due to the great technical challenges in simultaneously keeping the graphitization of the framework without oxidation, the orderliness of mesopores, the hydrophilicity, and the low toxicity of the nanosphere surfaces.

Recently, the combination of physically and biologically targeted drug delivery is one of the research directions for the treatment of tumors,[26] among which breast cancer is considered as the most common malignancy and the second main cause of cancer deaths in women today.[27] Especially, human epithelial growth factor receptor 2 (HER2) overexpressed breast cancer is reported to be particularly malignant.[28] Therefore, targeted drug delivery to HER2-positive breast cancer cells is of great importance for the therapy. A new peptide obtained *via* phage display technology exhibits excellent selectivity to HER2-positive human mammary carcinoma cells (SK-BR-3).[29] On one hand, this peptide, designated as SP13 in this work, was exploited as the biological targeting ligand for breast cancer. On the other hand, breast cancer is a kind of tumor that is well suited for NIR-induced photothermal therapy.

Herein, taking advantage of both biocompatible mesoporous silica and pristine mesoporous carbon, a peptide-conjugated core−shell graphitic carbon@silica nanosphere with dual-ordered mesopores, mesoporous carbon nanosphere@mesoporous silica-polyethylene glycol-SP13 (MMPS), was successfully fabricated. Its doxorubicin (DOX)-loaded form (MMPSD) could be applied for NIR/pH-responsive sustained-release and synergized targeted photothermal chemotherapy of breast cancer. A detailed illustration is shown in Scheme 1.

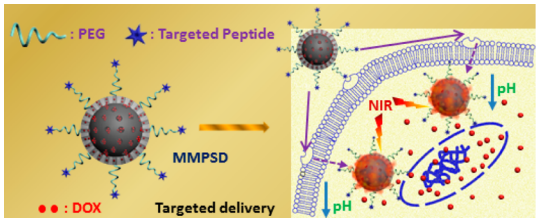

Scheme 1. Schematic representation of the sturcture of MMPSD and its application in NIR/pH-triggered, synergistic targeted photothermal chemotherapy.

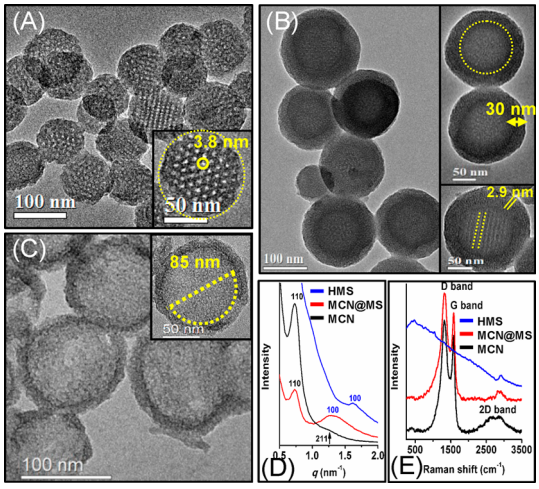

Figure 1. TEM and HRTEM (insets) images of MCN (A), MCN@MS (B), and HMS (C), respectively. SAXS patterns (D) and Raman spectra (E) of MCN (black), MCN@MS (red), and HMS (blue).

RESULTS AND DISCUSSION

Synthesis and Characterization of Different Vectors. MCN with an average diameter of ~90 nm (Figure S1) were synthesized according to a reported protocol with some modifications (Experimental Section (ES)).[30] Transmission electron microscopy (TEM) results showed that ordered mesopores were fitly distributed in spherical MCN, and the pore size was measured to be 3.8 nm (Figure 1A and S2A). Energy dispersive X-ray spectroscopy (EDX) analysis revealed that MCN were highly pure carbon with very little oxygen doping (Figure S3). The small-angle X-ray scattering (SAXS) pattern of MCN exhibited two resolved scattering peaks at q values of 0.73 and 1.27 nm, respectively (Figure 1D), which can be indexed as the typical (110) and (210) reflections of a highly ordered body-centered cubic $Im\bar{3}m$ mesostructure with a unit cell parameter (a_0) of 12.2 nm (Table S1). The N_2 adsorption−desorption isotherm and corresponding pore diameter distribution curve revealed that the

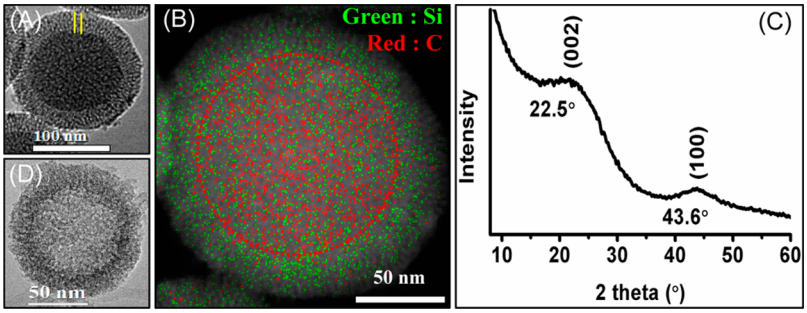

Figure 2. TEM image (A) and EDX mapping (B) of individual MCN@MS, XRD pattern of MCN@MS (C), and TEM image of an individual HMS (D).

MCN had a Brunauer–Emmett–Teller (BET) surface area of 864 $m^2\ g^{-1}$, a large pore volume of 0.94 $cm^3\ g^{-1}$, and a narrow pore size distribution centered at 3.8 nm (consistent with the TEM measurement) (Figure S4). The graphitization of MCN was proved by the Raman spectrum (Figure 1E), which gave obvious signals similar to the symmetry A_{1g} mode and E_{2g} mode of graphitic carbon atoms at 1330 cm^{-1} (D-band), 1580 cm^{-1} (G-band), and 2700 cm^{-1} (2D-band), respectively.[31] To synthesize core–shell graphitic carbon@silica nanospheres with dual-ordered mesopores (mesoporous carbon nanosphere@mesoporous silica, MCN@MS), an ordered mesoporous silica layer was uniformly coated on MCN by a surfactant (CTAB)-assisted approach (ES). The SAXS pattern of MCN@MS exhibited an additional scattering peak at a q value of 1.29 nm as compared to that of MCN (Figure 1D), proving the emergence of hexagonal *P6mm* mesostructure with a unit cell parameter (a_0) of 5.6 nm, while the IR spectrum also gave clear additional signals of amido-silica (Figure S6B). The scanning electron micrograph (SEM) image showed MCN@MS remained as nanospheres with a much larger diameter (~150 nm) than that of the MCN (Figure S1). TEM results of MCN@MS demonstrated that an ordered mesoporous layer with a pore size of 2.9 nm and thickness of 30 nm was well coated on the MCN and the core–shell structure can be clearly observed (Figures 1B, 2A, and S2B). It is of much interest that the mesoporous channels in the shell were almost vertical to the core surfaces (Figure 2A), which ensures the effective connection of the two kinds of ordered mesopores and also convenient mass transport between the core and shell. EDX analysis also accounted for the carbon-silica composite (Figure S3), and EDX mapping further validated the carbon@silica core–shell structure (Figure 2B). The similar Raman spectrum between the MCN and MCN@MS suggested that the graphitized structures were well retained during the coating process (Figure 1E). This can also be supported by the X-ray diffraction (XRD) pattern of MCN@MS (Figure 2C). It exhibited two resolved diffraction peaks at 2θ values of 22.5° and 43.6°, respectively, which can be indexed as the typical (002) and (100) reflections of graphitic carbon similar to the reduced graphene.[32,33] As compared to that of MCN, the N_2 adsorption–desorption isotherm revealed that MCN@MS had a BET surface area of 518 $m^2\ g^{-1}$ and pore volume of 0.71 $cm^3\ g^{-1}$, while the pore diameter distribution curve of MCN@MS exhibited an additional pore at 2.9 nm, attributed to the ordered mesoporous silica coating (Figure S4 and Table S1). The structure of core–shell nanospheres with dual-ordered mesopores was further evidenced by the calcination test (ES), which indicated that highly pure hollow mesoporous silica nanospheres (HMS) with an average diameter of ~125 nm could be obtained by combustion removal of MCN from MCN@MS (Figure 1 and Figures S1–S3). Notably, the smaller size of HMS as compared to MCN@MS was attributed to the shrinkage of the shell and pore under high-temperature calcination (Figure 2D). The content of MCN in MCN@MS was then calculated to be about 48.4 wt % by the thermogravimetric analysis (TGA) (Figure S5).

Due to the amido-mesoporous silica coating, MCN@MS can be easily modified with hydrophilic polyethylene glycol (PEG) to give MCN@MS-PEG (MMP) and then further conjugated with the targeting ligand SP13, obtaining MMPS (ES and Scheme 1). The successful PEGylation and SP13 modification were proven by FT-IR spectra (Figure S6) and zeta (ζ) potential analysis (Figure S7).

Water Dispersity and Hemolysis. The water dispersity measurement showed that both the mesoporous silica coating and the postmodification of PEG/SP13 resulted in increased water dispersity (Figure S7). For example, MMP, MMPS, and MMPSD solution did not apparently deposit until 180 h at the concentration of 50 μg/mL, which might be attributed to the hydrophilic modification with proper PEG densities.[34] The dynamic light scattering (DLS) curve showed that the MMPSD solution had a typical particle size of about 173 nm (Figure S8), only a little larger than that measured by TEM for MCN@MS (Figure S1B). This might be due to the PEG/SP13 modification and hydrophilization.[35] This phenomenon further confirmed the good water dispersity of MMPSD. Hemolytic tests indicated that the mesoporsous silica coating can significantly reduce the hemolysis to less than 5% even at a high concentration (1000 μg/mL) as compared with the

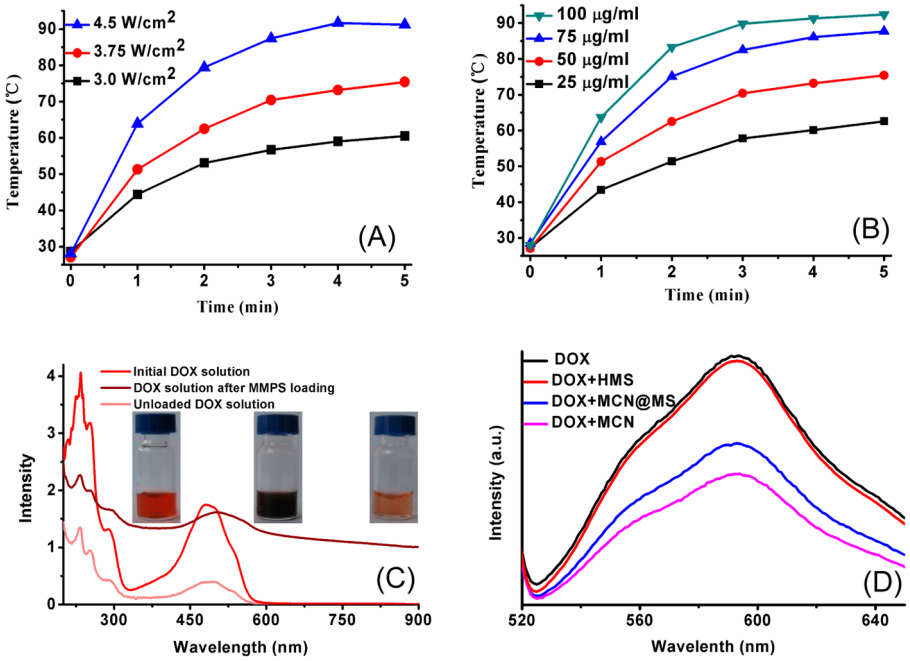

Figure 3. Photothermal heating curves of MMPS solution at various power intensities with an MCN@MS concentration of 50 μg/mL (A) and at various MCN@MS concentrations with a power intensity of 3.75 W/cm^2 (B). UV−vis spectra of DOX solution before and after loading into MMPS (diluted 5 times) (C). Fluorescence spectra of DOX solutions after different vector loadings. In these solutions, the initial DOX and vector concentrations were the same (D).

uncoated counterpart (Figure S9). The result accounted for the good biocompatibility of the core−shell nanoparticles.

Photothemal Heating Effect. The prepared materials exhibited strong NIR absorption at 808 nm and high NIR photothermal heating efficiency (Figure S10). As compared with the other two important high hydrophilic drug vectors such as MSN and oxidized mesoporous carbon nanoparticles (OMCN), MCN@MS exhibited much higher NIR absorption at 808 nm at the same concentration due to the absence of hotspots in MSN and the breakage of the graphitic framework in OMCN during the hydrophilization treatment (oxidization) (Figure S11A).[10,23] Therefore, MCN@MS showed faster temperature elevation with the increase of irradiation time than OMCN at the same MCN concentration (Figure S11B), while MSN cannot be used for photothermal heating. Furthermore, the coating and postmodification also resulted in an increased NIR absorption and photothermal heating efficiency due to the enhanced dispersity (Figure S10). For example, when irradiated by an 808 nm NIR laser at a power intensity of 3.75 W/cm^2, the MMPS solution temperature exceeded the biological cell photoablation limit of 50 °C within 1 min at the concentration of 50 μg/mL (Figure 3A). Moreover, MMPS exhibited a laser power intensity-dependent (Figure 3A) and concentration-dependent photothermal heating effect (Figure 3B and Table S2). These properties of MMPS will be beneficial for controllable photothermal therapy.

Drug Location. The hydrophobic core−hydrophilic shell structure with dual-ordered mesopores of MMPS is very suitable for the loading and release of hydrophobic drug molecules due to special interactions such as supramolecular π-stacking, van der Waals forces, and pore adsorption.[36] These interactions endow MMPS with high drug loading capacity (1.97 ± 0.28 mg/mg), with an entrapment efficiency of ~79% for aromatic DOX molecules, which was higher than those of uncoated MCN (1.60 ± 0.22 mg/mg) and OMCN (0.99 ± 0.25 mg/mg) (Table S2). The increased capacities might be attributed to the maintained graphitic π-structure and the elevated pore adsorption after mesoporous silica coating. UV−vis spectra showed that the intensity of characteristic absorption peaks of DOX markedly decreased in the solution after loading in MMPS, indicating that most DOX molecules were directly clustered into the dual-ordered mesopores (Figure 3C). Fluorescence spectra of different solutions that contained the same DOX and vector concentrations were used to investigate the location of DOX in MMPS (Figure 3D). The fluorescence intensity of the DOX solution after MCN loading (DOX+MCN) was much lower than that of pure DOX solution, while the intensity of DOX+HMS almost remained the same. This might be attributed to the fact that MCN, but not HMS, can cause fluorescence quenching by π-stacking of aromatic DOX molecules on graphitic carbon.[37] For DOX+MCN@MS, its fluorescence intensity was also much lower than that of DOX or DOX+HMS, but a little higher than that of DOX+MCN. Therefore, it

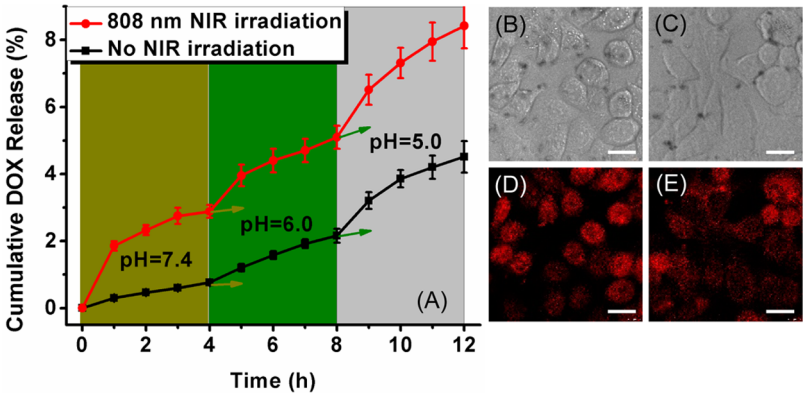

Figure 4. (A) Cumulative DOX release profiles from MMPSD under different pH values with or without 3.75 W/cm^2 NIR irradiation. Data are expressed as mean ± SEM (n = 3). (B–E) pH-stimulated release of DOX in SK-BR-3 cells. Cells were treated with MMPSD with an MCN@MS concentration of 50 μg/mL without (B, D) and with (C, E) pretreatment with bafilomycin A1. B and C are the corresponding bright field images of D and E. Red: DOX. Bar = 20 μm.

can be concluded that most of the adsorbed DOX molecules were loaded in the graphitic MCN cores by the hydrophobic interaction between DOX and graphitic carbon,[11] and also a few DOX molecules may be loaded in the mesoporous silica shell or adsorbed on the surface of MCN@MS by electrostatic interaction.[38]

Drug Release. As shown in Figure 4A, MMPSD exhibited desirable pH-dependent and NIR-mediated release behavior. The immediate contact between DOX molecules and hotspots facilitated the NIR-stimulated release. The enhanced release in low pH could be attributed to the reduced hydrophobic $\pi-\pi$ interaction between DOX and graphitic cores and decreased electrostatic interaction between DOX and the silica shells.[22,24] The responsive release behavior is favorable for cancer therapy because of the acidic cancer/cell microenvironment and convenient NIR implementation. Moreover, owing to the prolonged and narrowed drug release channels after coating, MMPSD exhibited a slower drug release rate as compared to the uncoated MCN or OMCN (Figure S12). This property, together with the high drug loading capacity, would meet the demand of sustained release. The pH-stimulated release of DOX from MMPSD was further confirmed with SK-BR-3 cells. Bafilomycin A1 is a widely used inhibitor of the vacuolar type H^+-ATPase (V-ATPase) and thereby efficiently prevents the acidification of lysosomes and increases the intralysosomal pH from ~5.3 to ~6.3.[39,40] As shown in Figure 4B–E, the pretreatment of bafilomycin A1 decreased the DOX fluorescent signal in most cells, indicating the pH-responsive release of DOX from MMPSD.

Targeted Delivery. Further studies were performed to verify the targeted delivery effect and also explore the preliminary mechanism of the drug delivery systems. Here, SK-BR-3 cells, known to have high expression of cell surface HER2 oncoprotein, were used as model cells, and nontumorigenic MCF-10A breast epithelial

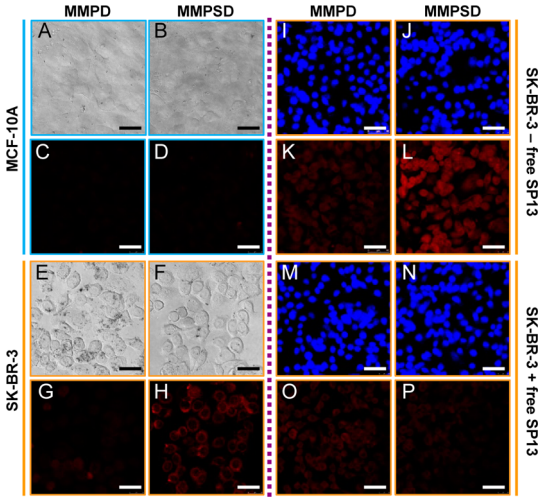

Figure 5. Cellular uptake of MMPD (without the SP13 ligand) and MMPSD (with the SP13 ligand) with an MCN@MS concentration of 50 μg/mL. The incubation time was 15 min (A–H) and 30 min (I–P), respectively. (A–D) MCF-10A cells, (E–P) SK-BR-3 cells, and (M–P) treated with competitive free SP13 peptide. A, B, E, and F are the corresponding bright-field images of C, D, G, and H. I, J, M, and N are the corresponding nucleus-stained images of K, L, O, and P. Blue: DAPI-stained nuclei; red: DOX. Bar = 50 μm.

cells, which have no significant HER2 expression, were used as control cells.[41] As shown in Figure 5, SP13-modified MMPSD exhibited markedly higher ability to deliver DOX to HER2-overexpressing SK-BR-3 cells than unmodified MMPD (Figure 5E–L). Both MMPD and MMPSD did not show apparent DOX delivery in MCF-10A cells (Figure 5A–D). These results demonstrated the targeting ability of SP13 to assist drug delivery systems to HER2-positive breast cancer cells. Moreover, the addition of a large amount of competing SP13 (Figure 5M–P) significantly inhibited the DOX uptake of SP13-modified MMPSD in SK-BR-3 cells (Figure 5P *vs* L), but had no apparent impact on that of MMPD (Figure 5O *vs* K). This is the typical phenomenon of

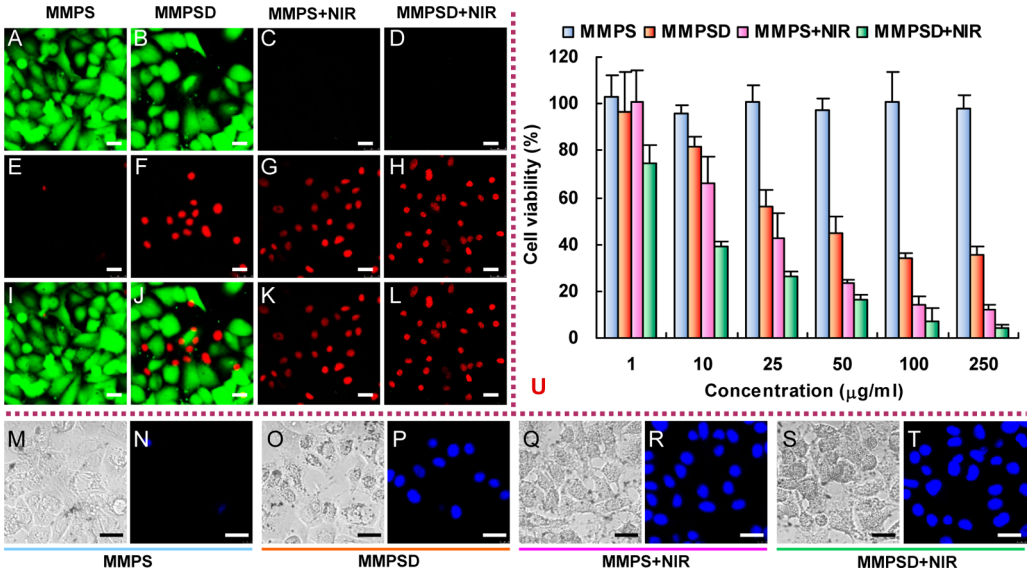

Figure 6. Evaluation of photothermal chemotherapeutic effect in SK-BR-3 cells. (A−L) Live−dead cell stain results, where I, J, K, and L are the corresponding merged images of A and E, B and F, C and G, and D and H. Green: live cells; red: dead cells. (M−T) Cell death results, when N, P, R, and T are the corresponding cell death images of M, O, Q, and S. Blue: DAPI-stained nuclei. Bar = 25 μm. (U) Cytotoxicity result evaluated *via* the CCK-8 test.

receptor-mediated competitive inhibition. As SP13 is considered as a specifically binding peptide to receptor HER2 on breast cancer cells,[29] the results implied that the peptide-receptor-mediated process might be one of the main mechanisms for cellular uptake of MMPSD, and the uptake was time-dependent (Figure 5E−L). When the incubation time reached 30 min, DOX delivered by MMPSD could reach the nuclei efficiently (Figure S13).

Combined Synergistic Therapy. The photothermal chemotherapeutic effect of the designed nanocarrier systems were evaluated *via* different means. As shown in Figure 6A−L, live−dead cell stain results indicated significantly higher cell death of NIR-irradiated photothermal treatment groups (Figure 6C/G/K and D/H/L) compared to the only chemotherapeutic treatment group (Figure 6B/F/J) due to the strong heat-induced damage, while very little cell death was observed in the DOX-free MMPS material group (Figure 6A/E/I) due to the biocompatible mesoporous silica coating and PEG modification.[42] This result was further confirmed when using DAPI dye to stain dead cells. More dead cells were observed in radiated groups compared to nonradiated groups (Figure 6M−T). In this work, NIR radiation not only triggered the release of DOX for enhanced chemotherapy (Figure 4) but also caused cell death itself for photothermal therapy (Figure 6). Furthermore, it has been reported that proper heating could increase the cell membrane permeability to enhance the intracellular delivery of drugs.[43] The cytotoxicity was further quantified *via* an accurate CCK-8 cell viability assay (Figure 6U). At each concentration, chemophotothermal therapy exhibited the highest cytotoxicity compared to single chemotherapy or photothermal therapy (Figure 6U). The IC_{50} values of different treatments are shown in Table S3. The quantification result showed that the IC_{50} of the photothermal chemotherapeutic group (MMPSD+NIR) was lower than that of the chemotherapeutic group (MMPSD) and the photothermal group (MMPS+NIR). The calculated combination index (CI) value was 0.422, indicating the synergistic photothermal chemotherapeutic effect of the MMPSD system.[44] Furthermore, it should be noted that the synergistic therapy resulted in a significantly lower IC_{50} of DOX (10.05 μg/mL) compared to that of free DOX (124.5 μg/mL). This also implied that MMPSD will be an efficient cancer-cell-killing platform.

CONCLUSIONS

A synergistic photothermal chemotherapeutic platform based on core−shell MCN@MS was prepared and then conjugated with PEG and SP13 peptide for enhanced DOX delivery. In this platform, the graphitic mesoporous carbon cores can not only load large amounts of the hydrophobic drug DOX in their hotspots but also effectively absorb and convert NIR energy into heat upon NIR laser irradiation. The hydrophilic mesoporous silica shell guarantees a good biocompatibility of the platform, easily functionalized surface, and effective mass transfer from core to shell. Owing to the unique structure including the immediate contact between the aromatic drug and the hotspots, the multifunctional system exhibited a high drug loading capacity, high targeting ability, sensitive NIR/pH-responsive DOX release, sustained release, and excellent combined cancer therapeutic effect for HER2-positive breast cancer. All these desirable

characteristics were concentrated in a single and easily fabricated smart drug delivery system, which presents an encouraging prospect for biomedical application and especially for cancer therapy.

EXPERIMENTAL SECTION

Materials. SP13 peptide (sequence: CAYQRFDDVASRF) was synthesized by Ziyu Biotechnology Co., Ltd. (Shanghai, China). Doxorubicin was purchased from Huafeng United Technology Co., Ltd. (Beijing, China). α-Malemidyl-ω-*N*-hydroxysuccinimidyl polyethylene glycol (MW 3500) was obtained from JenKem Technology Co., Ltd. (Beijing, China). Live−dead kits (catalogue no. R37601) were bought from Molecular Probes (Eugene, OR, USA). Cell Counting Kit-8 (CCK) was purchased from Dojindo Laboratories (Japan). 4′,6-Diamidino-2-phenylindole dihydrochloride (DAPI), triblock copolymer Pluronic F127, and aminopropyltriethoxysilane (APTES) were purchased from Sigma-Aldrich (St. Louis, MO, USA). Bafilomycin A1 from *Streptomyces griseus* was purchased from J&K Scientific Ltd. (Shanghai, China). Tetraethyl orthosilicate (TEOS) was purchased from Shanghai Lingfeng Chemical Co. Ltd. (China). Cetyltrimethylammonium bromide (CTAB), triethylamine, formaldehyde, sodium hydrate (NaOH), and other reagents, if not specified, were purchased from Sinopharm Chemical Reagent Co., Ltd. (China). All the chemicals were used without further purification.

Human mammary carcinoma SK-BR-3 cells and nontumorigenic MCF-10A breast epithelial cells were obtained from the America Type Culture Collection. SK-BR-3 cells were maintained in RPMI 1640 medium supplemented with 10% fetal bovine serum (FBS) and 1% penicillin−streptomycin. MCF-10A cells were cultured in Dulbecco's modified Eagle medium also supplemented with 10% FBS and 1% penicillin−streptomycin. Both cell lines were maintained at 37 °C under a 5% CO_2 atmosphere. The cell culture media and relating reagents were purchased from Gibco (Tulsa, OK, USA).

Synthesis of MSN, Graphitic MCN, and OMCN. MSN were prepared in our previous work.[45] The MCN used in this work were synthesized according to a reported protocol with some modifications.[30] Briefly, phenol (0.6 g), formalin aqueous solution (2.1 mL, 37 wt %), and NaOH aqueous solution (15 mL, 0.1 M) were mixed and stirred at 70 °C for 30 min to obtain low-molecular-weight phenolic resols. After that, triblock copolymer Pluronic F127 (0.96 g) dissolved in water (15 mL) was added. Then the mixture was stirred at 66 °C for 2 h. Water (50 mL) was added to the solution, which continued to agitate for 18 h. After cooling to room temperature, 260 mL of water was added to dilute the obtained solution. The diluent was transferred into an autoclave and heated at 130 °C for 24 h. The yellow powders were collected by centrifugation, washed with water, and freeze-dried. To obtain the graphitic MCN, the dry powders were graphitized under a highly pure N_2 atmosphere by temperature programming (25 °C → 350 °C for 60 min, 350 °C → 550 °C for 120 min, 550 °C → 750 °C for 120 min, 750 °C → 750 °C for 60 min). For the synthesis of OMCN, MCN were treated in an acid mixture (the volume ratio of H_2SO_4 to HNO_3 was 3) by ultrasound and stirring for 6 h. After that, OMCN were obtained by centrifugation and washing until the pH value of the spent liquor was neutral.

Synthesis of Amido-Mesoporous Silica Coated MCN (MCN@MS). Briefly, 3 mg of MCN was dispersed in CTAB aqueous solution (30 mL, 1 mg/mL) by strong ultrasonication for 2 h. NaOH solution (0.4 mL, 0.1 M) was added, and the resulting solution was heated to 60 °C. TEOS (30 μL) and ethanol (120 μL) were subsequently added, and the solution was stirred at 60 °C. After that, an APTES−ethanol solution (5 μL + 60 μL) (APTES was not added for the synthesis of MCN@MS without amination) was added, and the mixture continued to stir at 60 °C for 30 min. Then, the solution was kept still at 60 °C for 24 h. The solid product was recovered by centrifugation and washing. To remove CTAB from the pores, MCN@MS was repeatedly refluxed in a mixture of methanol and NH_4NO_3 (2 mg/mL).

Functionalization of MCN@MS. To synthesize PEGylated MCN@MS (MMP), 2 mg of MCN@MS was dispersed in 3.35 mL of phosphate-buffered solution (PBS, pH 8.0) by sonication, and bifunctional PEG−PBS solution (4 mL, 1 mg/mL, pH 8.0) was added. Then, the mixture was stirred at room temperature for 2 h. The solid product was recovered by centrifugation and washing. For the synthesis of SP13-modified MMP (MMPS), the above prepared MMP were dispersed in SP13-PBS solution (2 mL, 0.5 mg/mL, pH 7.0) and stirred at room temperature for 18 h. The resulting MMPS were also purified *via* centrifugation.

Characterization of Therapeutic Vectors. Transmission electron microscopy , high-resolution TEM, and energy dispersive X-ray spectroscopy experiments were performed on JEM-2010 instruments with an acceleration voltage of 200 kV. For TEM observation, the samples were dispersed in ethanol and supported on a holey carbon film on a Cu grid. Scanning electron micrographs were obtained on a Philips XL-30 scanning electron microscope operating at 20 kV. The particle size distribution was counted statistically according to the SEM images. Small-angle X-ray scattering measurements were taken on a Nanostar U SAXS system (Bruker, Germany) using Cu Kα radiation (40 kV, 35 mA). X-ray diffraction patterns were obtained with a Rigaku D/MAX-RB diffractometer by using Cu Ka radiation at 40 kV and 60 mA. Raman spectra was taken on a Labram-1B (Dilor, France) Raman spectrometer with a 632.8 nm wavelength incident laser light. N_2 adsorption−desorption isotherms at 77 K and pore size distribution curves were measured using Tristar 3000 systems. Before measurements, the samples were degassed under vacuum at 300 °C for at least 12 h. The BET method was used to calculate the surface area. Thermogravimetric analysis (TGA) was carried out on a Pyris Diamond TG thermogravimetric analyzer (PerkinElmer Thermal Analysis). The sample was heated from room temperature to 800 °C at 5 °C/min under an air atmosphere. Fourier transform infrared (FT-IR) spectroscopy was obtained from a Nicolet-670 FTIR spectrometer using the KBr pellet method. Ultraviolet−visible absorption spectra (UV−vis) were obtained on a UV−vis absorption spectrometer (UV759, China). The mean diameter and zeta potential of MSN/MCN-based systems were determined by DLS using a Malvern NanoZS zeta potential/particle sizer. Optical photographs of different sample solutions were taken using a common Canon camera.

Fluorescence Spectrum to Investigate DOX Location in MCN@MS. The HMS, MCN, and MCN@MS with the same HMS or MCN amount were separately soaked in DOX aqueous solution (1 mL, 0.5 mg/mL) and stirred in the dark at room temperature for 12 h, respectively. Then, the mixtures and the pure DOX solution (0.5 mg/mL) were equally diluted and measured on a fluorescent spectrophotometer. The DOX location in MCN@MS was determined by comparing the fluorescence intensity of different diluents.

Hemolysis Assay. Hemolysis assay was performed to evaluate the biocompatibility of different materials.[46] To harvest erythrocytes, sterile defibrinated sheep blood was centrifuged at 3000 rpm for 5 min. The cell pellet was washed three or four times with saline and thereafter resuspended in saline to achieve a concentration of 2% (v/v). Different materials were dissolved in saline and diluted to different concentrations from 0.1 to 1000 μg/mL. For each concentration, 150 μL of test solution was mixed with 150 μL of 2% erythrocytes. The resulting mixture was incubated in a water bath for 1 h at 37 °C and further centrifuged at 3000 rpm for 15 min. The release of hemoglobin in the supernatant was determined by photometric analysis at 540 nm. The hemolytic percentage was calculated as follows: hemolytic percentage (%) = $(OD_{test} - OD_{saline})/(OD_{H2O} - OD_{saline}) \times 100\%$.

Photothermal Heating Effect. Different vectors were dispersed in PBS (pH 7.4) with an MCN or MCN@MS concentration of 50 μg/mL for comparison of the photothermal heating effect,

and PBS (pH 7.4) was used as the negative control. A 200 μL solution was placed in a 96-well plate and then irradiated with an 808 nm NIR laser (3.75 W/cm^2) for different time periods. To determine the impact of NIR power density on the photothermal heating effect, an MMPS solution with an MCN@MS concentration of 50 μg/mL was irradiated under different power densities. To investigate the impact of concentration on the photothermal heating effect, MMPS with different MCN@MS concentrations were prepared and irradiated with an 808 nm laser at 3.75 W/cm^2. Solution temperature was monitored by an accurate digital thermometer immediately after irradiation.

Preparation of DOX-Loaded Delivery Systems. To load DOX, the above prepared MCN, OMCN, MMP, or MMPS were soaked in DOX aqueous solution (10 mL, 1 mg/mL) and stirred in the dark at room temperature for 12 h. Then, 2.4 μL of triethylamine was added, and the mixture was stirred for another 12 h. After that, the mixture was centrifuged and the supernatant was removed. The DOX-loaded delivery systems were washed with water to remove the loosely adsorbed DOX on the surface. Finally, the drug delivery systems were resuspended in PBS (pH 7.4) at proper concentration for further experiments.

Loading Capacity and Entrapment Efficiency. During the preparation of DOX-loaded delivery systems, the removed supernatants were collected for quantitative analysis of unloaded DOX by UV−vis spectroscopy. To calculate the loading capacity and entrapment efficiency, the standard curve of DOX was established. Loading capacity (mg/mg) = mass of loaded DOX (mg)/mass of MCN@MS (mg). Entrapment efficiency (%) = [mass of loaded DOX (mg)/mass of added DOX (mg)] $\times$ 100%.

***In Vitro* Release.** First, MMPSD (containing 100 μg of MCN@MS) was dispersed in 0.5 mL of PBS (pH 7.4) and agitated at 300 rpm. The mixture was centrifuged at each hour point. The supernatant (200 μL) was taken for DOX detection, and the same volume of fresh buffer was added back to the residual mixture. At the fourth and eighth hour point, the solvents were changed to PBS (pH 6.0) and PBS (pH 5.0), respectively. The cumulative DOX release from different vectors (MMPS, MCN, and OMCN) for comparison was also carried out by this method under constant pH = 6.0. For the NIR-triggered release experiment, the mixture was irradiated with an 808 nm NIR laser (3.75 W/cm^2) for 5 min at each hour point. The amount of released DOX was measured using an Agilent Cary Eclipse fluorescence spectrophotometer. The cumulative release of DOX was determined as a percentage compared to the loaded DOX within MMPSD.

pH-Stimulated Release of DOX within Cells. To evaluate the pH-stimulated release of DOX within SK-BR-3 cells, bafilomycin A1, an inhibitor of V-ATPase was introduced to prevent the acidification of lysosomes.[39] SK-BR-3 cells were cultured in 96-well microplates with 100 μL of media at a density of 1.2 $\times$ 10^4 cells/well for 2 days. After rinsing with PBS, the wells were pretreated with 80 μL of bafilomycin A1 (100 nM) for 1 h. Then MMPSD with an MCN@MS concentration of 250 μg/mL (20 μL) was added into the wells and incubated for 30 min. Subsequently, wells were rinsed carefully with PBS and fixed with 4% paraformaldehyde for 15 min, after which the medium was changed to PBS. Control wells without pretreatment with bafilomycin A1 were treated in parallel. Confocal microscopy was performed using a Leica TCs SP5 microscope equipped with a Leica application suite. Repetitive studies were carried out, and three independent fields were observed in each study.

Targeting Ability Evaluation. Confocal microscopy was used to determine the targeting ability of different systems in different cell lines. SK-BR-3 and MCF-10A cells were cultured in 96-well microplates with 100 μL of media at a density of 1.2 $\times$ 10^4 cells/well and 1 $\times$ 10^4 cells/well for 2 days, respectively. After rinsing with PBS, MMPD and MMPSD with an MCN@MS concentration of 50 μg/mL were added into the wells and incubated for 15 min. Then the cells were rinsed carefully with PBS and fixed with 4% paraformaldehyde for 15 min, after which the medium was changed to PBS. Confocal microscopy was performed as described above to determine the targeting ability of different drug delivery systems.

Competitive Inhibition Study. To preliminarily evaluate the cellular uptake mechanism of drug delivery systems, a competitive inhibition experiment was performed. SK-BR-3 cells were cultured in 96-well microplates with 100 μL of media at a density of 1.2 $\times$ 10^4 cells/well for 2 days. After rinsing with PBS, MMPD and MMPSD with an MCN@MS concentration of 50 μg/mL were incubated with cells for 30 min. For the inhibition group, significantly excessive SP13 (5 mg/mL) was preincubated with the cells for 15 min. After fixing with 4% paraformaldehyde for 15 min, DAPI solution (0.5 μg/mL) was added to stain the nuclei for 10 min. Confocal microscopy was performed as described above to determine the cellular uptake of different drug delivery systems after different treatments.

Qualitative Evaluation of Photothermal Chemotherapeutic Effects. Two independent experiments were performed to qualitatively evaluate the photothermal chemotherapeutic effects against breast cancer cells. (1) Live−dead kits were applied to visualize cell death using a confocal microscope. SK-BR-3 cells were maintained in 96-well microplates with 100 μL of media at a density of 1 $\times$ 10^4 cells per well for 2 days. After washing with PBS, MMPS and MMPSD with an MCN@MS concentration of 50 μg/mL were incubated with cells for 4 h. For the photothermal groups, wells were irradiated with an 808 nm NIR laser (3.75 W/cm^2) for 5 min. Following that, the culture media was replaced with a fresh one and the cells were cultured for another 12 h. Then the cells were stained using live−dead kits according to the manufacturer's instructions. Confocal microscopy was carried out when live cells exhibited a green color and dead ones showed a red color. (2) DAPI-indicated apoptosis was evaluated to determine the combined therapeutic effect. SK-BR-3 cells were maintained in 96-well microplates with 100 μL of media at a density of 1.2 $\times$ 10^4 cells per well for 48 h. Treatments were carried out similarly to that in the live−dead experiment. Cells were incubated with MMPS or MMPSD for 3 h. After washing, another 4 h incubation was performed. Immediately after incubation, cells were rinsed with PBS carefully and stained using DAPI for 10 min. Then confocal microscopy was performed. For both experiments, repetitive studies were carried out and three independent fields were observed in each study.

Quantitative Evaluation of Photothermal Chemotherapeutic Effects. CCK-8 was applied to quantitatively determine photothermal chemotherapeutic effects against breast cancer cells under different treatments. SK-BR-3 cells were cultured in 96-well microplates with 100 μL of media at a density of 1 $\times$ 10^4 cells/well for 2 days. After washing with PBS, a series of concentrations of free DOX, MMPS, and MMPSD solutions were incubated with cells for 3 h. For the photothermal groups, wells were irradiated with an 808 nm NIR laser (3.75 W/cm^2) for 5 min. The culture media was replaced with a fresh one, and the cells were cultured for another 4 h. After that, 10 μL of CCK-8 solution was added to each well and incubated for another 2 h at 37 °C. The absorbance was measured with a microplate reader at 450 nm. Viability of treated cell wells was expressed as a percentage of the viability of unexposed wells. All experiments were carried out in quadruplicate.

Calculation of Combination Index. The combination index was calculated to evaluate the combination effect of chemotherapy and photothermal therapy according to previous work.[44] $CI = D_1/Df_1 + D_2/Df_2 + D_1D_2/(Df_1Df_2)$. In this work, Df_1 is the IC_{50} of DOX in the chemotherapy and D_1 is the IC_{50} of DOX in the combined therapy. Correspondingly, Df_2 is the IC_{50} of MCN@MS in the photothermal therapy and D_2 is the IC_{50} of MCN@MS in the combined therapy. The value of CI represents different meanings (CI < 1: synergism, CI > 1: antagonism, CI = 1: additive effects).

Conflict of Interest: The authors declare no competing financial interest.

Acknowledgment. This work was supported by grants from National Key Basic Research Program (2013CB932502) of China (973 Program), the National Natural Science Foundation of China (21303022), "Zhuo Xue" Talent Plan of Fudan University, Natural Science Foundation of Shanghai City of China (13ZR1451400), and Sino-German Research Project (GZ995). E.W. also appreciates receiving a Fudan University Key Laboratory Senior Visiting Scholarship.

Supporting Information Available: Further characterizations such as SEM, TEM, and HRTEM images, EDX patterns, N_2

adsorption−desorption isotherm, pore size distribution curve, TGA curve, IR spectra, optical images, zeta potentials, hemolysis, UV−vis spectra, photothermal heating curves, release profiles, and intracellular localization images are given in Figures S1−S13. This material is available free of charge *via* the Internet at http://pubs.acs.org.

REFERENCES AND NOTES

1. Chung, C.; Kim, Y. K.; Shin, D.; Ryoo, S. R.; Hong, B. H.; Min, D. H. Biomedical Applications of Graphene and Graphene Oxide. *Acc. Chem. Res.* **2013**, *46*, 2211–2224.
2. Lee, S. M.; Park, H.; Choi, J. W.; Park, Y. N.; Yun, C. O.; Yoo, K. H. Multifunctional Nanoparticles for Targeted Chemo-photothermal Treatment of Cancer Cells. *Angew. Chem., Int. Ed.* **2011**, *50*, 7581–7586.
3. Dong, K.; Liu, Z.; Li, Z.; Ren, J.; Qu, X. Hydrophobic Anticancer Drug Delivery by a 980 nm Laser-Driven Photothermal Vehicle for Efficient Synergistic Therapy of Cancer Cells *in Vivo*. *Adv. Mater.* **2013**, *25*, 4452–4458.
4. Zhang, Z.; Wang, J.; Chen, C. Near-Infrared Light-Mediated Nanoplatforms for Cancer Thermo-Chemotherapy and Optical Imaging. *Adv. Mater.* **2013**, *25*, 3869–3880.
5. Nam, J.; La, W. G.; Hwang, S.; Ha, Y. S.; Park, N.; Won, N.; Jung, S.; Bhang, S. H.; Ma, Y. J.; Cho, Y. M.; *et al*. pH-Responsive Assembly of Gold Nanoparticles and "Spatiotemporally Concerted" Drug Release for Synergistic Cancer Therapy. *ACS Nano* **2013**, *7*, 3388–3402.
6. Zhang, Z. J.; Wang, J.; Chen, C. Y. Near-Infrared Light-Mediated Nanoplatforms for Cancer Thermo-Chemotherapy and Optical Imaging. *Adv. Mater.* **2013**, *25*, 3869–3880.
7. Yang, K.; Feng, L. Z.; Shi, X. Z.; Liu, Z. Nano-Graphene in Biomedicine: Theranostic Applications. *Chem. Soc. Rev.* **2013**, *42*, 530–547.
8. Mao, H. Y.; Laurent, S.; Chen, W.; Akhavan, O.; Imani, M.; Ashkarran, A. A.; Mahmoudi, M. Graphene: Promises, Facts, Opportunities, and Challenges in Nanomedicine. *Chem. Rev.* **2013**, *113*, 3407–3424.
9. Feng, L. Y.; Wu, L.; Qu, X. G. New Horizons for Diagnostics and Therapeutic Applications of Graphene and Graphene Oxide. *Adv. Mater.* **2013**, *25*, 168–186.
10. Robinson, J. T.; Tabakman, S. M.; Liang, Y. Y.; Wang, H. L.; Casalongue, H. S.; Vinh, D.; Dai, H. J. Ultrasmall Reduced Graphene Oxide with High Near-Infrared Absorbance for Photothermal Therapy. *J. Am. Chem. Soc.* **2011**, *133*, 6825–6831.
11. Kim, H.; Lee, D.; Kim, J.; Kim, T.; Kim, W. J. Photothermally Triggered Cytosolic Drug Delivery *via* Endosome Disruption Using a Functionalized Reduced Graphene Oxide. *ACS Nano* **2013**, *7*, 6735–6746.
12. Duch, M. C.; Budinger, G. R. S.; Liang, Y. T.; Soberanes, S.; Urich, D.; Chiarella, S. E.; Campochiaro, L. A.; Gonzalez, A.; Chandel, N. S.; Hersam, M. C.; *et al*. Minimizing Oxidation and Stable Nanoscale Dispersion Improves the Biocompatibility of Graphene in the Lung. *Nano Lett.* **2011**, *11*, 5201–5207.
13. Wang, Y.; Wang, K. Y.; Zhao, J. F.; Liu, X. G.; Bu, J.; Yan, X. Y.; Huang, R. Q. Multifunctional Mesoporous Silica-Coated Graphene Nanosheet Used for Chemo-Photothermal Synergistic Targeted Therapy of Glioma. *J. Am. Chem. Soc.* **2013**, *135*, 4799–4804.
14. Bitounis, D.; Boucetta, H. A.; Hong, B. H.; Min, D. H.; Kostarelos, K. Prospects and Challenges of Graphene in Biomedical Applications. *Adv. Mater.* **2013**, *25*, 2258–2268.
15. Li, M.; Yang, X. J.; Ren, J. S.; Qu, K. G.; Qu, X. G. Using Graphene Oxide High Near-Infrared Absorbance for Photothermal Treatment of Alzheimer's Disease. *Adv. Mater.* **2012**, *24*, 1722–1728.
16. Chng, E. L.; Pumera, M. The Toxicity of Graphene Oxides: Dependence on the Oxidative Methods Used. *Chem.—Eur. J.* **2013**, *19*, 8227–8235.
17. Seabra, A. B.; Paula, A. J.; de Lima, R.; Alves, O. L.; Duran, N. Nanotoxicity of Graphene and Graphene Oxide. *Chem. Res. Toxicol.* **2014**, *27*, 159–168.
18. Magrez, A.; Kasas, S.; Salicio, V.; Pasquier, N.; Seo, J. W.; Celio, M.; Catsicas, S.; Schwaller, B.; Forro, L. Cellular Toxicity of Carbon-Based Nanomaterials. *Nano Lett.* **2006**, *6*, 1121–1125.
19. Song, G. S.; Wang, Q.; Wang, Y.; Lv, G.; Li, C.; Zou, R. J.; Chen, Z. G.; Qin, Z. Y.; Huo, K. K.; Hu, R. G.; Hu, J. Q. A Low-Toxic Multifunctional Nanoplatform Based on Cu_9S_5@$mSiO_2$ Core-Shell Nanocomposites: Combining Photothermal- and Chemotherapies with Infrared Thermal Imaging for Cancer Treatment. *Adv. Funct. Mater.* **2013**, *23*, 4281–4292.
20. Fang, W. J.; Yang, J.; Gong, J. W.; Zheng, N. F. Photo- and pH-Triggered Release of Anticancer Drugs from Mesoporous Silica-Coated Pd@Ag Nanoparticles. *Adv. Funct. Mater.* **2012**, *22*, 842–848.
21. Fang, W.; Tang, S.; Liu, P.; Fang, X.; Gong, J.; Zhen, N. Pd Nanosheet-Covered Hollow Mesoporous Silica Nanoparticles as a Platform for the Chemo-Photothermal Treatment of Cancer Cells. *Small* **2012**, *8*, 3816–3822.
22. Zhang, Z.; Wang, L.; Wang, J.; Jiang, X.; Li, X.; Hu, Z.; Ji, Y.; Wu, X.; Chen, C. Mesoporous Silica-Coated Gold Nanorods as a Light-Mediated Multifunctional Theranostic Platform for Cancer Treatment. *Adv. Mater.* **2012**, *24*, 1418–1423.
23. Wang, Y.; Wang, K. Y.; Yan, X. Y.; Huang, R. Q. A General Strategy for Dual-Triggered Combined Tumor Therapy Based on Temple Semigraphitized Mesoporous Silica Nanoparticles. *Adv. Healthcare Mater.* **2014**, *3*, 485–489.
24. Zhu, J.; Liao, L.; Bian, X. J.; Kong, J. L.; Yang, P. Y.; Liu, B. H. pH-Controlled Delivery of Doxorubicin to Cancer Cells, Based on Small Mesoporous Carbon Nanospheres. *Small* **2012**, *8*, 2715–2720.
25. Karavasili, C.; Amanatiadou, E. P.; Sygellou, L.; Giasafaki, D. K.; Steriotis, T. A.; Charalambopoulou, G. C.; Vizirianakis, I. S.; Fatouros, D. G. Development of New Drug Delivery System Based on Ordered Mesoporous Carbons: Characterisation and Cytocompatibility Studies. *J. Mater. Chem. B* **2013**, *1*, 3167–3174.
26. Wagner, E. Programmed Drug Delivery: Nanosystems for Tumor Targeting. *Expert. Opin. Biol. Ther.* **2007**, *7*, 587–593.
27. Gonzalez-Angulo, A. M.; Morales-Vasquez, F.; Hortobagyi, G. N. Overview of Resistance to Systemic Therapy in Patients with Breast Cancer. *Adv. Exp. Med. Biol.* **2007**, *608*, 1–22.
28. Corsi, F.; Fiandra, L.; De-Palma, C.; Colombo, M.; Mazzucchelli, S.; Verderio, P.; Allevi, R.; Tosoni, A.; Nebuloni, M.; Clementi, E.; *et al*. HER2 Expression in Breast Cancer Cells Is Downregulated upon Active Targeting by Antibody-Engineered Multifunctional Nanoparticles in Mice. *ACS Nano* **2011**, *5*, 6383–6393.
29. Wang, J.; Dong, B.; Chen, B.; Jiang, Z.; Song, H. Selective Photothermal Therapy for Breast Cancer with Targeting Peptide Modified Gold Nanorods. *Dalton Trans.* **2012**, *41*, 11134–11144.
30. Fang, Y.; Gu, D.; Zou, Y.; Wu, Z. X.; Li, F. Y.; Che, R. C.; Deng, Y. H.; Tu, B.; Zhao, D. Y. A Low-Concentration Hydrothermal Synthesis of Biocompatible Ordered Mesoporous Carbon Nanospheres with Tunable and Uniform Size. *Angew. Chem., Int. Ed.* **2010**, *49*, 7987–7991.
31. Wang, Y.; Sun, H.; Zhang, R.; Yu, S. N.; Kong, J. L. Large Scale Templated Synthesis of Single-Layered Graphene with a High Electrical Capacitance. *Carbon* **2013**, *53*, 245–251.
32. Wang, G. X.; Yang, J.; Park, J. S.; Gou, X. L.; Wang, B.; Liu, H.; Yao, J. Facile Synthesis and Characterization of Graphene Nanosheets. *J. Phys. Chem. C* **2008**, *112*, 8192–8195.
33. Nethravathi, C.; Rajamathi, M. Chemically Modified Graphene Sheets Produced by the Solvothermal Reduction of Colloidal Dispersions of Graphite Oxide. *Carbon* **2008**, *46*, 1994–1998.
34. Natte, K.; Österle, W.; Friedrich, J. F.; Klitzing, R.; Orts-Gil, G. Tuning Interfacial Properties and Colloidal Behavior of Hybrid Nanoparticles by Controlling the Polymer Precursor. *Macromol. Chem. Phys.* **2012**, *213*, 2412–2419.
35. Gillich, T.; Acikgöz, C.; Isa, L.; Dieter Schlüter, A.; Spencer, N. D.; Textor, M. PEG-Stabilized Core-Shell Nanoparticles: Impact of Linear *versus* Dendritic Polymer Shell Architecture on Colloidal Properties and the Reversibility of

Temperature-Induced Aggregation. *ACS Nano* **2013**, *7*, 316–329.
36. Luo, Z.; Ding, X. W.; Hu, Y.; Wu, S. J.; Xiang, Y.; Zeng, Y. F.; Zhang, B. L.; Yan, H.; Zhang, H. C.; Zhu, L. L.; *et al*. Engineering a Hollow Nanocontainer Platform with Multifunctional Molecular Machines for Tumor-Targeted Therapy *in Vitro* and *in Vivo*. *ACS Nano* **2013**, *7*, 10271–10284.
37. Nakayama-Ratchford, N.; Bangsaruntip, S.; Sun, X. M.; Welsher, K.; Dai, H. J. Noncovalent Functionalization of Carbon Nanotubes by Fluorescein-Polyethylene Glycol: Supramolecular Conjugates with pH-Dependent Absorbance and Fluorescence. *J. Am. Chem. Soc.* **2007**, *129*, 2448–2449.
38. Tang, S. H.; Huang, X. Q.; Chen, X. L.; Zheng, N. F. Hollow Mesoporous Zirconia Nanocapsules for Drug Delivery. *Adv. Funct. Mater.* **2010**, *20*, 2442–2447.
39. Fischer, S.; Ronellenfitsch, M. W.; Thiepold, A. L.; Harter, P. N.; Reichert, S.; Kögel, D.; Paschke, R.; Mittelbronn, M.; Weller, M.; Steinbach, J. P.; *et al*. Hypoxia Enhances the Antiglioma Cytotoxicity of B10, a Glycosylated Derivative of Betulinic Acid. *PLoS One* **2014**, *9*, e94921.
40. Yoshimori, T.; Yamamoto, A.; Moriyama, Y.; Futai, M.; Tashiro, Y. Bafilomycin A1, a Specific Inhibitor of Vacuolar-Type H^+-ATPase, Inhibits Acidification and Protein Degradation in Lysosomes of Cultured Cells. *J. Biol. Chem.* **1991**, *266*, 17707–17712.
41. Do, M. T.; Hwang, Y. P.; Kim, H. G.; Na, M.; Jeong, H. G. Mollugin Inhibits Proliferation and Induces Apoptosis by Suppressing Fatty Acid Synthase in HER2-Overexpressing Cancer Cells. *J. Cell. Physiol.* **2013**, *228*, 1087–1097.
42. Singh, N.; Karambelkar, A.; Gu, L.; Lin, K.; Miller, J. S.; Chen, C. S.; Sailor, M. J.; Bhatia, S. N. Bioresponsive Mesoporous Silica Nanoparticles for Triggered Drug Release. *J. Am. Chem. Soc.* **2011**, *133*, 19582–19585.
43. Wang, C.; Xu, H.; Liang, C.; Liu, Y.; Li, Z.; Yang, G.; Cheng, L.; Li, Y.; Liu, Z. Iron Oxide@Polypyrrole Nanoparticles as a Multifunctional Drug Carrier for Remotely Controlled Cancer Therapy with Synergistic Antitumor Effect. *ACS Nano* **2013**, *7*, 6782–6795.
44. Liu, S. H.; Guo, Y. B.; Huang, R. Q.; Li, J. F.; Huang, S. X.; Kuang, Y. Y.; Han, L.; Jiang, C. Gene and Doxorubicin Co-Delivery System for Targeting Therapy of Glioma. *Biomaterials* **2012**, *33*, 4907–4916.
45. Wang, Y.; Shi, W.; Song, W. S.; Wang, L.; Liu, X. G.; Chen, J.; Huang, R. Q. Tumor Cell Targeted Delivery by Specific Peptide-Modified Mesoporous Silica Nanoparticles. *J. Mater. Chem.* **2012**, *22*, 14608–14616.
46. Huang, R. Q.; Han, L.; Li, J. F.; Liu, S. H.; Shao, K.; Kuang, Y. Y.; Hu, X.; Wang, X. X.; Lei, H.; Jiang, C. Chlorotoxin-Modified Macromolecular Contrast Agent for MRI Tumor Diagnosis. *Biomaterials* **2011**, *32*, 5177–5186.